V-type Asteroids as the Origin of Mesosiderites

Guy Libourel, Pierre Beck, Akiko M Nakamura, Pierre Vernazza, Clément Ganino, Patrick Michel

The Planetary Science Journal, 4:123 (12pp), 2023 July https://doi.org/10.3847/PSJ/ace114

V-type Asteroids as the Origin of Mesosiderites

Guy Libourel[1], Pierre Beck[2], Akiko M. Nakamura[3], Pierre Vernazza[4], Clement Ganino[5], and Patrick Michel[1]
[1] Université Côte d'Azur, Lagrange, Observatoire de la Côte d'Azur, CNRS, Nice, France
[2] UJF-Grenoble 1/CNRS-INSU, Institut de Planétologie et d'Astrophysique de Grenoble, Grenoble, France
[3] Graduate School of Science, Kobe University, Japan
[4] Université Aix-Marseille, CNRS, Laboratoire d'Astrophysique de Marseille, Marseille, France
[5] Université Côte d'Azur, Géoazur, Observatoire de la Côte d'Azur, CNRS, Valbonne, France
Received 2023 January 13; revised 2023 June 17; accepted 2023 June 19; published 2023 July 14

Abstract

We present the results of a campaign of hypervelocity impact experiments on natural mesosiderite targets, using representative main asteroid belt impact speeds. The objective is to document further the surface evolution of iron-rich asteroids. In contrast with iron meteorites, we demonstrate the fragile behavior of mesosiderite at impact since experiments result in both cratering and catastrophic disruption. The behavior of metal-rich asteroids at impact is thus highly influenced by the original ratio of metal/silicate. A visible to near-infrared spectral analysis shows that the pyroxene silicate signature of impacted mesosiderites, or their ejecta, is fully preserved. Our results thus rule out a mesosiderite hypothesis for the very nature of M/X-type asteroids including (16) Psyche, despite a small fraction of its surface possibly being covered by mesosiderite-like materials. Finally, we address the question of whether mesosiderites and howardite–eucrite–diogenite (HED) meteorites are genetically linked to (4) Vesta or other differentiated asteroids in the main belt based on their spectral similarity.

Unified Astronomy Thesaurus concepts: Asteroids (72)

1. Introduction

Following endeavors on describing, understanding, and modeling the surface evolution of iron-rich asteroids subject to impacts at typical asteroid impact speeds (Libourel et al. 2019; Marchi et al. 2020; Maurel et al. 2020; Ogawa et al. 2021; Raducan et al. 2020), we present here new results obtained from hypervelocity impact experiments on mesosiderites. Mesosiderites are one of the most enigmatic groups of differentiated meteorites (Mittlefehldt 1990, 1994). They are breccias consisting of almost equal amounts of silicates and FeNi metals, plus some sulfides. Unlike pallasites, where the silicates, mainly olivines, are consistent with a mantle origin, the silicate fractions are largely basalts, gabbros, and pyroxenites with minor amounts of dunite and infrequent anorthosite (Scott et al. 2001). The silicates consist of mineral and lithic clasts set in a fine-grained fragmental to impact melt matrix. Mineral clasts consist of coarse-grained orthopyroxene, plagioclase, and rare olivine. The silicates are very similar to the howardite–eucrite–diogenite (HED) suite meteorites (McCord et al. 1970). Likewise, their oxygen isotopic compositions are indistinguishable from those of HED meteorites (e.g., Greenwood et al. 2006). FeNi metals in mesosiderites are mostly in the form of millimeter or submillimeter grains that are intimately mixed with similarly sized silicate grains. The metal compositions of mesosiderites display a chondritic siderophile element composition and are almost uniform, suggesting that they originate from the metallic core of a differentiated asteroid that was molten when mixed with the silicates (Hassanzadeh et al. 1990).

Previously proposed formation processes either consider the metal originating from the same parent body as the mesosiderite silicates (internal origin, e.g., Haba et al. 2019) or deriving from the core of a different asteroid that collided with the silicate parent body (external origin, e.g., Wasson & Rubin 1985; Rubin & Mittlefehldt 1992; Scott et al. 2001). Recently, high-precision uranium–lead dating of mesosiderite zircons have revealed that (4) Vesta in the inner main asteroid belt is the parent body of mesosiderite silicates (Haba et al. 2019). These authors have indeed shown that mesosiderite formation on (4) Vesta can be explained by a hit-and-run collision 4,525.4 million years ago that caused the thick crust observed by NASA's Dawn mission and explains the missing olivine in mesosiderites, HED meteorites, and vestoids. In particular, this chronological study reveals initial crust formation $4{,}558.5 \pm 2.1$ million years ago and metal–silicate mixing at $4{,}525.39 \pm 0.85$ million years. Implying a formation process that requires contributions from crust and core materials without mantle materials, mesosiderites provide unique insights into the catastrophic breakup of differentiated asteroids.

Asteroid (16) Psyche, the target of the NASA Psyche mission, is one of the very few main-belt asteroids that exhibits a relatively high radar albedo (Shepard et al. 2010, 2015) and shallow phase polarization minimum (Dollfus et al. 1979; Dollfus & Geake 1977), which imply that its surface/subsurface is metal rich. It is considered one of the few main-belt bodies that could have an exposed protoplanetary metallic core and that would thus be related to iron meteorites. Such an inference is however challenged by both its near-infrared (NIR) and mid-infrared spectral properties (Fornasier et al. 2010; Hardersen et al. 2005; Landsman et al. 2018; Ockert-Bell et al. 2010; Takir et al. 2016) and the reported estimates of its density around 3.8 ± 0.5 kg/m^3 (Drummond et al. 2018; Ferrais et al. 2020; Hanuš et al. 2017; Shepard et al. 2017; Vernazza et al. 2021; Viikinkoski et al. 2018; Elkins-Tanton et al. 2022). Considering that the densities of mesosiderites are similar to that of Psyche, assuming ∼20% microporosity, it has been proposed that Psyche could be a plausible candidate parent

body for mesosiderites (Viikinkoski et al. 2018), following the initial hypothesis based on numerical simulations (Davis et al. 1999). More recently, longitude–latitude maps of the thermal inertia and dielectric constant of Psyche derived from Atacama Large Millimeter/submillimeter Array data, have revealed that the surface of Psyche is heterogeneous in composition and structure. The surface signatures are suggestive of various proportions of metal- and silicate-rich materials with distinctive thermal-inertia properties and indicative of an evolved surface processed by impacts (Cambioni et al. 2022; de Kleer et al. 2021; see also Libourel et al. 2019; Marchi et al. 2020; Raducan et al. 2020).

However, it is very unlikely that any kind of meteorite comes from (16) Psyche given that this asteroid is not the parent body of a collisional family. As many large "isolated" bodies (i.e., without a family), it is not the best target from which to get meteorites. Since there are many M types with spectral properties like those of Psyche, we will use often M/X-type asteroids throughout the text rather than only (16) Psyche, with a regular emphasis on Psyche's physical properties as it is one of the three best characterized M types along with (22) Kalliope and (216) Kleopatra.

More generally, craters on a small body constitute an important source of information to estimate (1) the surface age relative to other planetary bodies, (2) the chronology of events that shaped the asteroid, (3) the environment in which the body evolved (Ogawa et al. 2021) and (4) the composition and strength of its subsurface (Maurel et al. 2020). However, the understanding of impacts on M/X-type asteroids (DeMeo & Carry 2014) poses an additional challenge since we are lacking a well-documented database of impact experiments and simulations on targets that can represent such bodies. Since both the size and shape of a crater are affected by the nature of the asteroid's surface (Jutzi et al. 2015; Marchi et al. 2016), calibrations against well-known crater size distributions may not apply optimally to metal-rich asteroids. An important effort in understanding cratering processes in metal-rich material, through a combination of impact experiments and simulations, is therefore crucial for the interpretation of telescopic and mission data of asteroids. In order to complement previous impact experiments on iron-rich materials, i.e., CrMo alloy steel, FeNi ingots, and iron meteorites, we conducted a campaign of hypervelocity impact experiments on mesosiderite targets, using representative main asteroid belt impact speeds in the range of 5 km s^{-1} (Bottke et al. 1994).

2. Samples, Experiments, and Analytical Methods

2.1. Samples

The mesosiderite SAH 98088 (Grossman 1999) has been selected as a representative sample of the mesosiderite class of meteorites for this set of hypervelocity impact experiments. It was indeed possible to have access to two pieces of SAH 98088 that are large enough to allow two-stage light-gas gun shots. FeNi metals, representing almost half of the modal proportion of the specimen and mostly in the form of millimeter or submillimeter grains, are intimately mixed with similarly sized silicate grains, although centimeter-sized nodules are common (Figure 1). The silicate portion is composed of orthopyroxene of rather uniform composition (circa $Wo_3En_{63}Fs_{34}$) and calcium-rich plagioclase of somewhat variable composition ($An_{86\text{-}92}$). Two chunks of SAH 98088 (Figure 1; meso#1 = 260 g and meso#2 = 232 g) have been used as targets. Shots were carried out on flat and polished surfaces.

2.2. Experiments

Two hypervelocity impact experiments were performed using a 7 mm bore two-stage light-gas gun at the Institute of Space and Astronautical Science (ISAS) in Japan. Cylindrical basaltic projectiles, similar to those used in previous impact experiments of metallic targets (Ogawa et al. 2021), of 3.2 mm in diameter, 2.3 mm in height, and 0.045 g in mass, were shot vertically at the mesosiderite target surface using a plastic sabot (Figure 1; Kawai et al. 2010). The impact velocity was 5.32 km s^{-1} on the meso#1 target and 3.34 km s^{-1} on the meso#2 target. Both experiments were performed under vacuum conditions (1.5 Pa) and at room temperature. Projectile and ejecta trajectories were captured with a high-speed video camera (frame rate of 2 or 100 μs^{-1}) that monitored the experiments (Figures 2 and 3).

2.3. Analytical Methods

Mineralogy. The description of targets before and after impact were performed using both the COXEM EM-30PLUS bench-top scanning electron microscope (SEM) at the Lagrange Laboratory of CNRS, located at the Observatoire de la Côte d'Azur, Member of Université Côte d'Azur. Both secondary and back scattered electron modes were used for images. Energy-dispersive X-ray diffraction (EDX) was used to analyze the target compositions.

Reflectance spectra were obtained with the SHADOWS instrument (Potin et al. 2018) at the Institut de Planétologie et d'Astrophysique of Grenoble. The system was used in standard beam configuration (roughly 6 mm diameter beam) and spectra were obtained under nadir illumination and a 30° emergence angle (phase = 30°). The spectra were normalized with respect to Spectralon™ and Infragold™ and were corrected for the non-Lambertian behavior of the Spectralon™. Only reflectance spectra on the meso#2 target and its fragments have been analyzed.

In order to compare the reflectance spectra of the mesosiderite cratering experiments to relevant planetary materials, we computed a number of spectral metrics. The pyroxene crystal field transition bands were analyzed by means of the band center, band depth, and band area with the definitions used in Moskovitz et al. (2010). Chiefly, the band center is calculated with a continuum removal for Band I (unlike Band II), and the red wing for Band II is calculated up to 2.45 μm. Band I and Band II refer in this study to the two strong absorption bands centered around 0.9 and 2 μm, respectively, which are typical of pyroxene.

2.4. Spectral Modeling

Spectral modeling of metal–eucrite mixtures was performed using intimated and geographic mixtures models. The end-member spectra of the metals were obtained from spectra of metal-alloy powders from the RELAB database. The end-member spectrum for the eucrite was selected as that of Millbillillie eucrite, also from the RELAB database. The geographic mixture simulates the coexistence of large areas covered by metallic and/or eucrite composition, and the spectrum of the mixture should then be a linear combination of

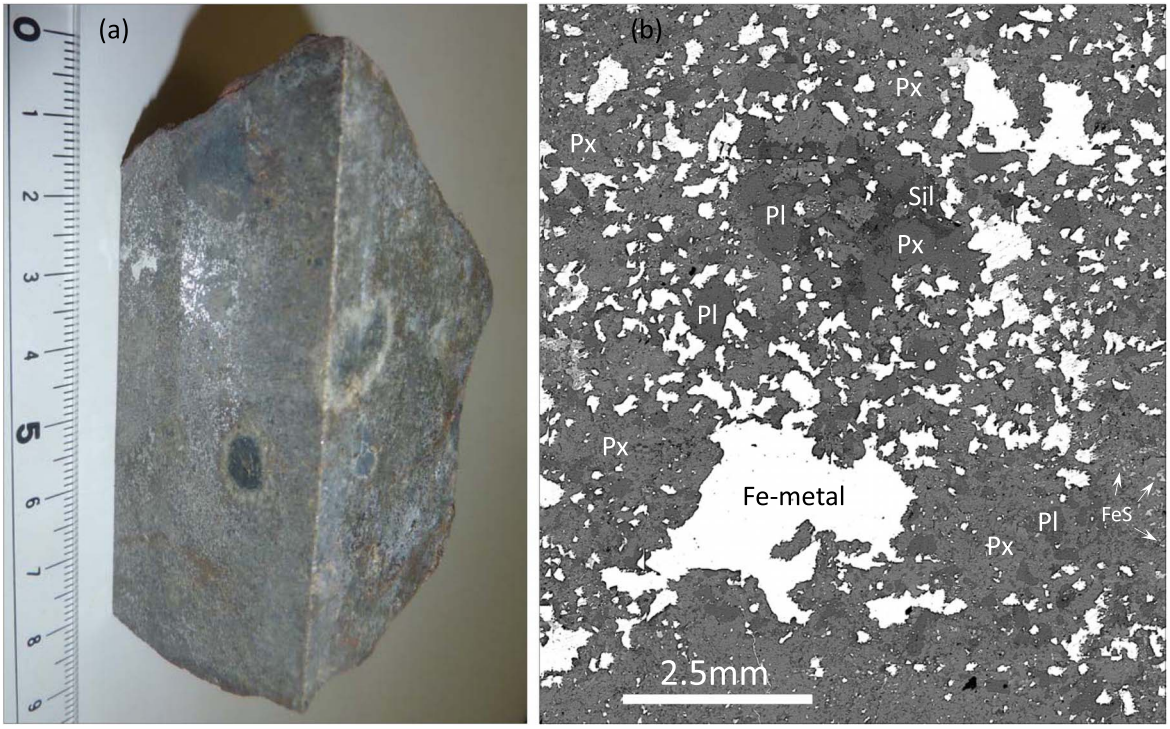

Figure 1. (a) Macroscopic and (b) microscopic views of the mesosiderite SAH 98088 sample used as a target for this set of hypervelocity impact experiments; here, the truncated sample is meso#1 = 232 g. Notice in both pictures the intimate mixtures between the silicates and FeNi metal phases. Shots have been carried out on flat and polished surfaces. Abbreviations: Px: pyroxene; Pl: plagioclase; FeS: iron sulfide; and Sil: silica-rich phase.

the two end-members, weighted by the fractional surface area coverage. The intimated mixture is calculated by first computing the single-scattering albedo spectrum of each end-member (see Pommerol & Schmitt 2008), mixing them linearly (then supposing similar grains sizes), and then computing the reflectance from the single-scattering albedo spectrum of the mixture.

3. Results

3.1. Hypervelocity Impact Experiments

The impact experiment at 3.34 km s^{-1} results in the formation of a 2 cm diameter irregular crater on the meso#2 target surface. The crater is intersected by several large cracks, some of which are radially distributed (Figure 2(a)). Since the target was small enough, the stress wave reflected at the free surfaces, including the rear surface of the target, causing spallation and affecting the shape of the spallation zone of the front surface, i.e., the crater shape. Despite its fracturation, the target nevertheless retains good overall cohesion, suggestive of a cratering impact regime. No trace of melt was detected inside the crater. High-speed camera images captured the sequence of the almost instantaneous stream of ejecta. Just after the hypervelocity impact (within just a few μs, Figure 2(b)), the stream is dominated by high-velocity fine-grained ejecta forming a typical cone-shaped curtain centered on the impact point. Coarser and heterogeneous grains follow in the ejection stream, which ends with millimeter to centimeter-sized ejecta (Figures 2(c)–(d)).

The shot performed at 5.32 km s^{-1} blasted completely the mesosiderite target (meso#1), indicative of a catastrophic disruption regime (Figure 3(a)). In contrast with the previous shot, high-speed camera images show that the mesosiderite target instantly lost its internal cohesion and broken up into a multitude of chunks of variable size (Figures 3(b–d)). The systematic search by SEM for traces of melting on the different disrupted fragments proved unsuccessful.

3.2. Laboratory vis–NIR Spectral Observations

The reflectance spectra measured outside of the cratered area on the saw-cut meso#2 mesosiderite reveal the presence of two strong absorption bands centered around 0.9 and 2 μm, typical of pyroxene, hereafter referred to as Band I and Band II, respectively. The exact position of the bands is suggestive of a relatively low Ca pyroxene, and the positions, depths, and area ratios of the bands are within the ranges found for mesosiderites, with values similar to howardites as well (see for instance Beck et al. 2011; Hiroi et al. 1995).

In Figures 4 and 5, all reflectance spectra obtained are presented. They include spectra measured within the crater, as well as spectra of ejecta of different granulometry (coarse grained, i.e., millimeter sized, and fine grained, i.e., $<$1 mm). At first order, it is shown that such impact craters do not erase the mafic signatures of mesosiderites, both in the impact crater or the ejected material. Variations in overall reflectance are observed when comparing the various spectra obtained, as well as in term of band depth and position. The two spectra obtained of the sawed surface outside of the impact crater are similar. Two of the spectra obtained within the crater are brighter than the uncratered saw-cut surface, which may be due to fragmentation of the silicate fraction within the crater, leading to more scattering of the incoming light.

The spectra obtained of the ejecta seem darker than the spectra of the craters and the original sample, but the pyroxene band depth remains strong, and the band positions stay within the range found for mesosiderites. The darkness of the ejecta

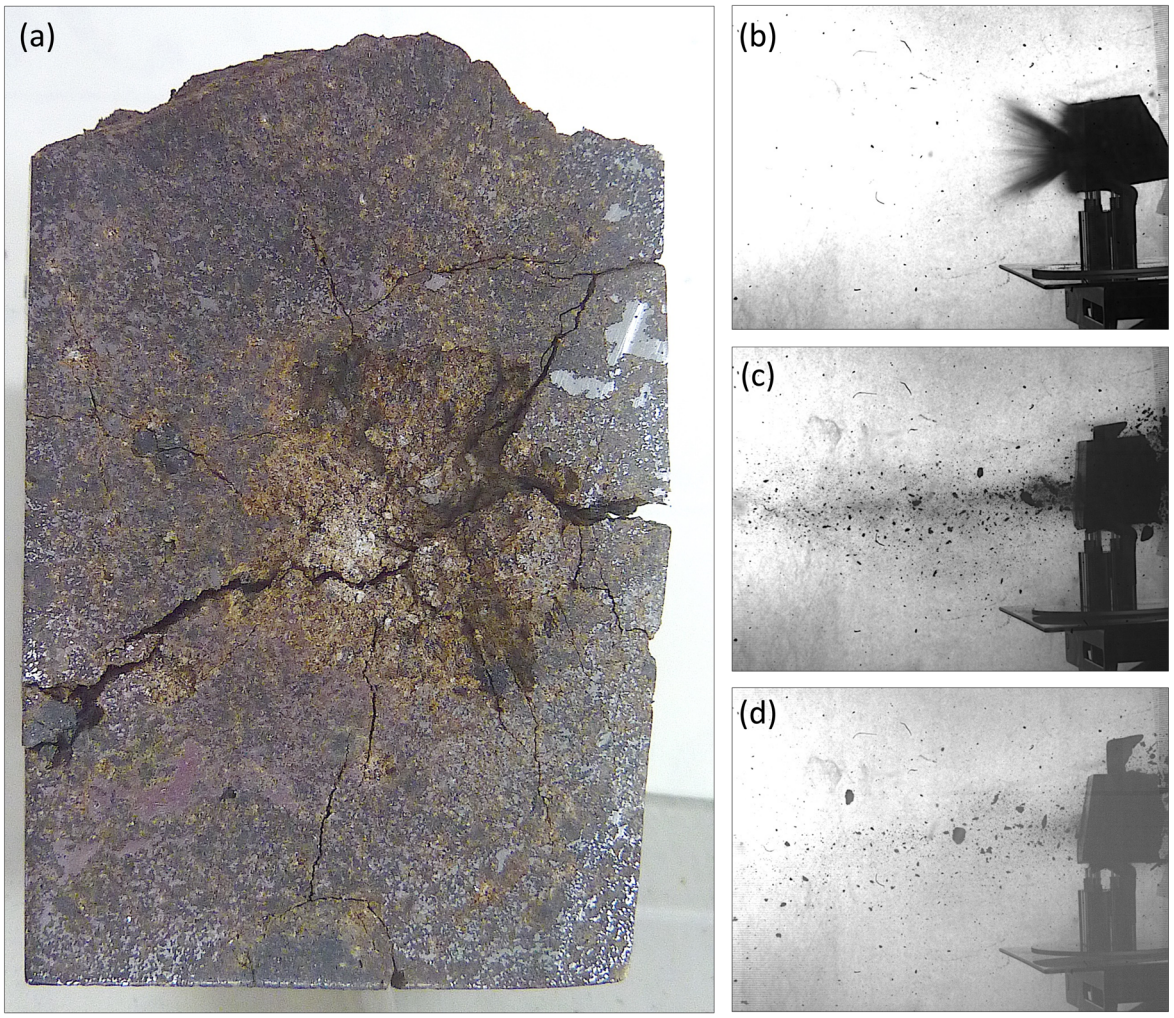

Figure 2. (a) 2 cm irregular crater on the meso#2 target surface after impact experiments at 3.34 km s^{-1}. No trace of melt has been detected inside the crater. High-speed camera images captured at (b) 0.1 ms, (c) 2.2 ms, and (d) 5.0 ms after impact (see the text for an explanation).

could be related to their modification in response to dynamical compression, but a simpler explanation is likely. The ejecta are rougher than the original material (saw cut), causing shadows and a decrease of reflectance for our spectra measured at a 30° phase angle.

It also appears that the position of Band I varies among the spectra obtained in these cratering experiments, while the value of the Band II position is relatively constant (Figure 6). This may be related to the contribution of iron oxyhydroxide to the spectra, which may impact the visible slope as well as the position of the 0.9 μm band. Overall, the variability observed is small; spectra of both the crater and the ejecta resemble spectra of the meteorite prior impact, with a strong low Ca pyroxene signature. Also, overall, the spectra and calculated spectral parameters are similar when comparing the spectra obtained of the crater and ejecta to other spectra obtained of mesosiderite powders and slabs.

4. Discussion

The outcome of our impact experiments on mesosiderites and their comparison to those on purely metal-rich objects have many implications regarding their different behaviors at impact and the signatures they leave on their fragments and surfaces, with implications on the linkage of asteroids in the belt to differentiated parent bodies. We discuss these in the following.

4.1. Cratering versus Disruptive Regime for Metal-rich Asteroids

Our study shows that metal-rich asteroids can respond very differently to collisions, depending on their actual metallic properties. Impact experiments on fully metal-rich targets (Libourel et al. 2019; Marchi et al. 2020; Matsui & Schultz 1984; Ogawa et al. 2021) showed that these targets have a ductile or brittle behavior, depending on the temperature of the environment. In all cases, they break into molten ejecta and their surfaces can experience a mineralogical transformation due to the impact of the projectile (Libourel et al. 2019). More precisely, basaltic projectiles lead to a coating on the metallic surface formed by a glassy silicate skin, resulting in an effect of camouflage of otherwise metallic asteroids. This may explain the lack of identified metallic objects in the asteroid belts, and the silicate band found for some M/X-type asteroids. For the range of impact speeds covered by those experiments, which are consistent with impact speeds in the asteroid belt, fully metallic targets only experienced cratering and fracturation but not a disruption.

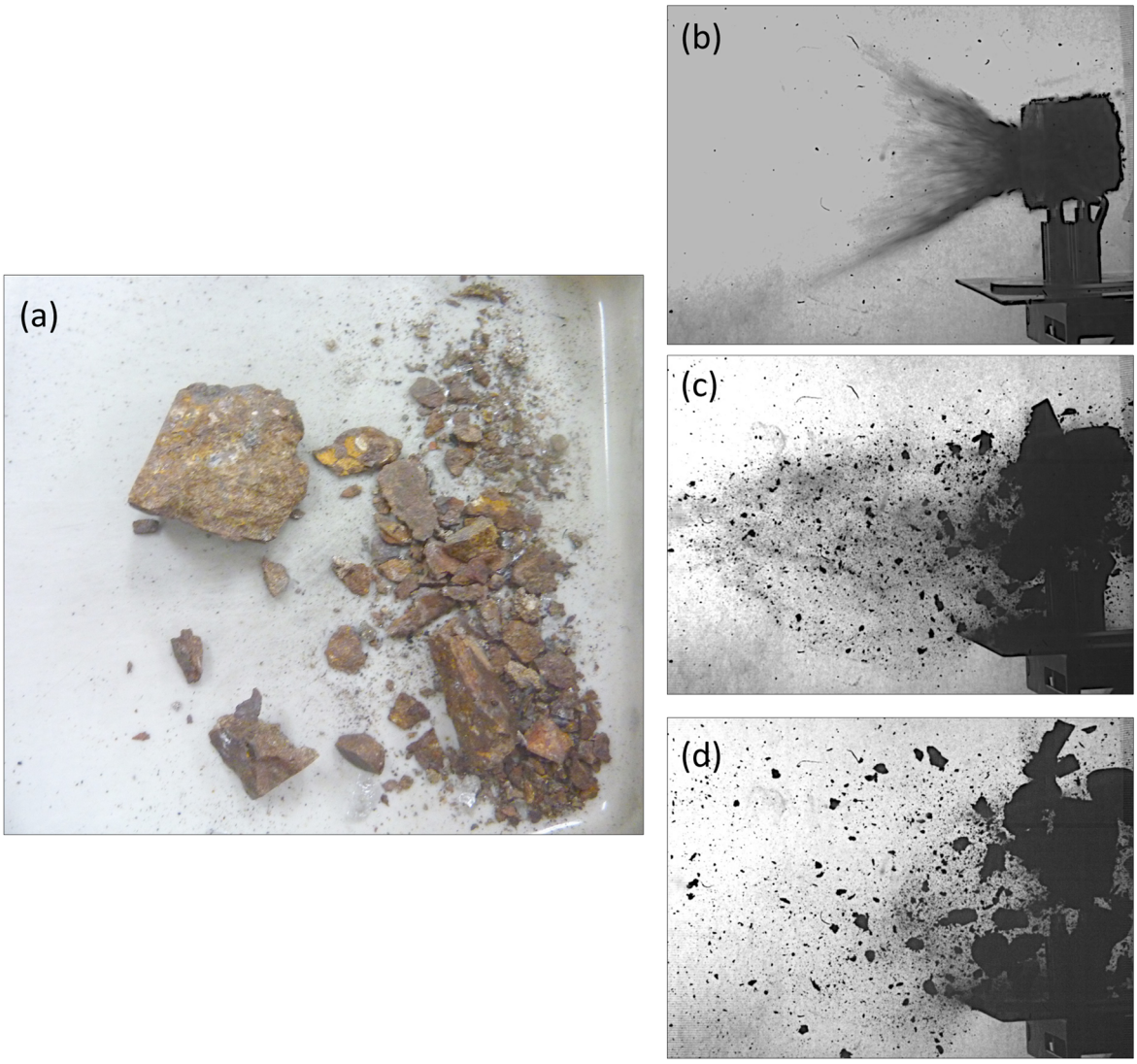

Figure 3. Debris and ejecta of variable size collected after impacts performed at 5.32 km s^{-1} on the meso#1 target. High-speed camera images captured the complete blasting of the meso#1 sample at (b) 0.1 ms, (c) 2.2 ms, and (d) 5.0 ms after impact.

On the other hand, our impact experiments on mesosiderites reveal their fragile behavior at impact since experiments result in both cratering and disruption (Figures 1 and 2). The specific energy, i.e., the ratio of the kinetic energy of the projectile to the mass of the target (generally denoted as Q) was 2.4×10^3 and 1.1×10^3 J kg^{-1} for meso#1 and meso#2, respectively. The largest fragment mass fraction to the original target mass f was 0.45 and 0.90, respectively, which means the shattering specific energy, i.e., the specific energy at which $f = 0.5(Q \times S)$ was $\sim 2 \times 10^3$ J kg^{-1} for mesosciderite, which is much lower than for metal targets (larger than 10^4 J kg^{-1}; Holsapple et al. 2002; Katsura et al. 2014) but rather close to those of ordinary chondrites (1.4×10^3 J kg^{-1}; Flynn et al. 2018). The impact-induced crack growth preferentially occurs in the weak part of the target, within and between silicate grains or the interface between silicate grains and metals (e.g., Michikami et al. 2019). Hence, the shattering specific energy Q^* may not be too different from that of ordinary chondrites. However, note that the two natural targets used in this experiment may have happened to be exceptionally fragile and more experiments should be conducted to show the reproducibility of these results. Moreover, the major ejecta collected are similar to the target, and do not experience any transformation. No trace of impact melt has been observed in this set of hypervelocity experiments, neither on ejecta nor at the crater floor. Although metamorphism may have occurred near the impact point, such small amounts of material would not remain inside the crater as in the case of metal targets but would be ejected at high velocity as fine grains (Ganino et al. 2019) and scattered into the chamber, where they would not be recovered. The silicate-rich nature of an impacted mesosiderite, or its ejecta, is fully preserved if not enhanced in our cratering experiments.

The behavior of metallic asteroids at impact is thus highly influenced by the original ratio of metal/silicate. Such a ratio can be variable and has some implications not only for mesosiderite bodies but also for pallasites (which will be the subject of a future study). This ratio also plays a critical role in the nature, properties, and evolution of surface regolith, both in terms of spectral characteristics and in mechanical and structural ones. The images that the Psyche mission may obtain of the surface of Psyche will allow us to shed some light on this dependency.

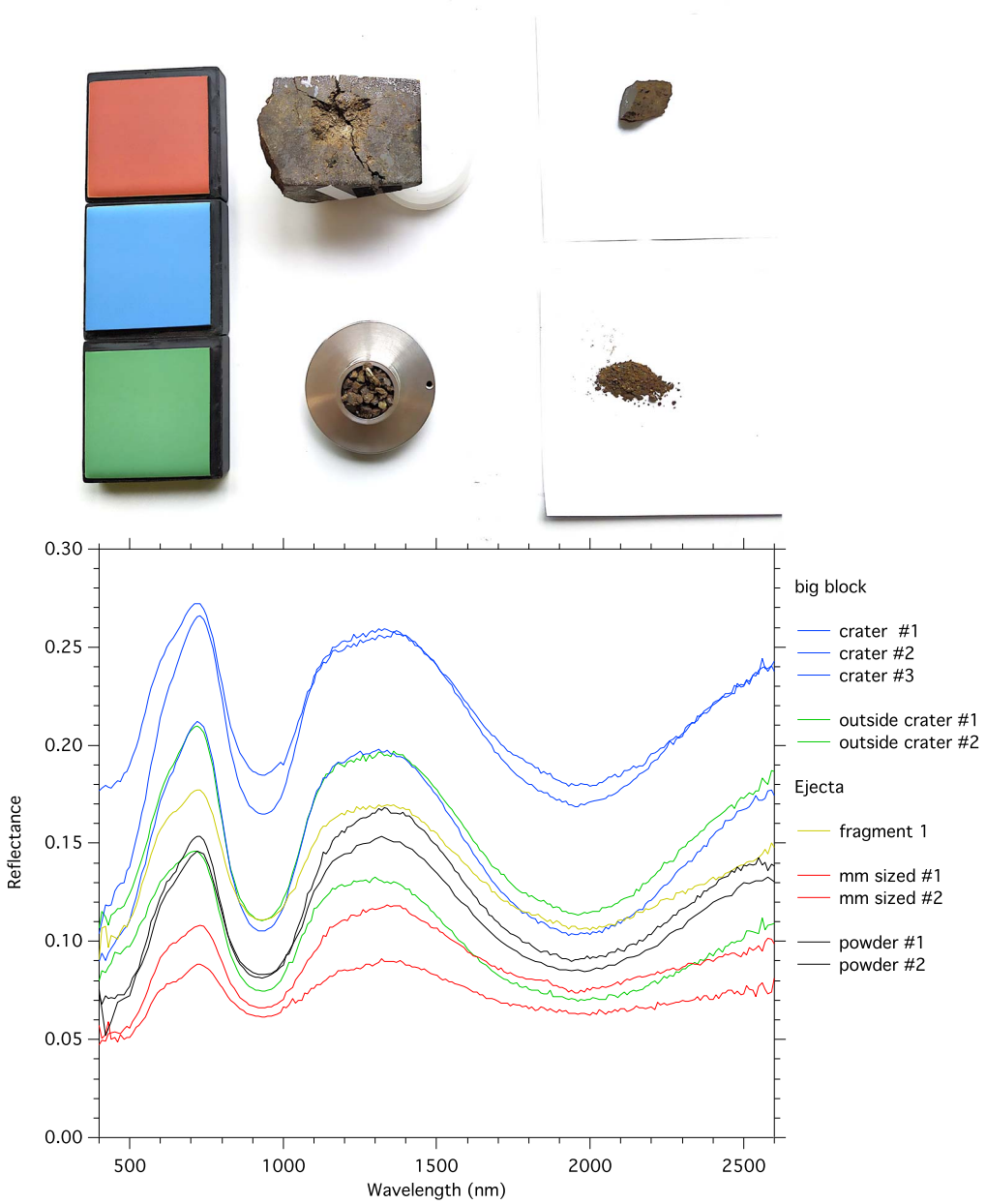

Figure 4. Visible to NIR (vis–NIR) spectra of samples subjected to hypervelocity impacts, of craters, debris, and ejecta, as labeled. The spectra were obtained under nadir illumination and a 30° emergence angle (phase = 30°).

4.2. The Surface of Psyche Does Not Look Like Mesosiderites and Is Pyroxene Poor

The spectra obtained were classified following the DeMeo et al. (2009) scheme using the tool smass.mit.edu/busdemeoclass.html. All spectra (crater, ejecta, and original sample) resulted in a classification as V type. In Figure 7, we compare our spectra to the V-type end-member from DeMeo et al. (DeMeo et al. 2009). This graph puts in light the remarkable similarity between the spectra obtained during the mesosiderite crater experiments and the V-type spectral end-member. Our results suggest that mesosiderite parent bodies may be searched among V-type asteroids, and that asteroid projectiles in the size range investigated here impacting a mesosiderite's surface may not erase this spectral classification. Solar-wind-related space weathering may change the spectra of a mesosiderite's surface (see Vernazza et al. 2009) but in a manner similar to that of HED meteorites and thus V types.

Because mesosiderites were suggested to be possibly associated to the large M-type (16) Psyche, we compare the spectra obtained in our study to available ground-based observations of (16) Psyche (Figure 7). While there are hints of absorption at 0.9 and 2 μm in the (16) Psyche spectra that point toward the presence of some amount of pyroxene on the surface of Psyche, the depth of the band is extremely small compared to our mesosiderite spectra. This comparison seems to rule out the mesosiderite hypothesis for the nature of Psyche (Viikinkoski et al. 2018). A similar conclusion had been proposed based on a comparison between the visible and NIR spectral properties of a chip of the Vaca Muerta mesosiderite (Vernazza et al. 2009) and those of M-type asteroids with faint 0.9 and 2.0 μm absorption features. It may still be that a

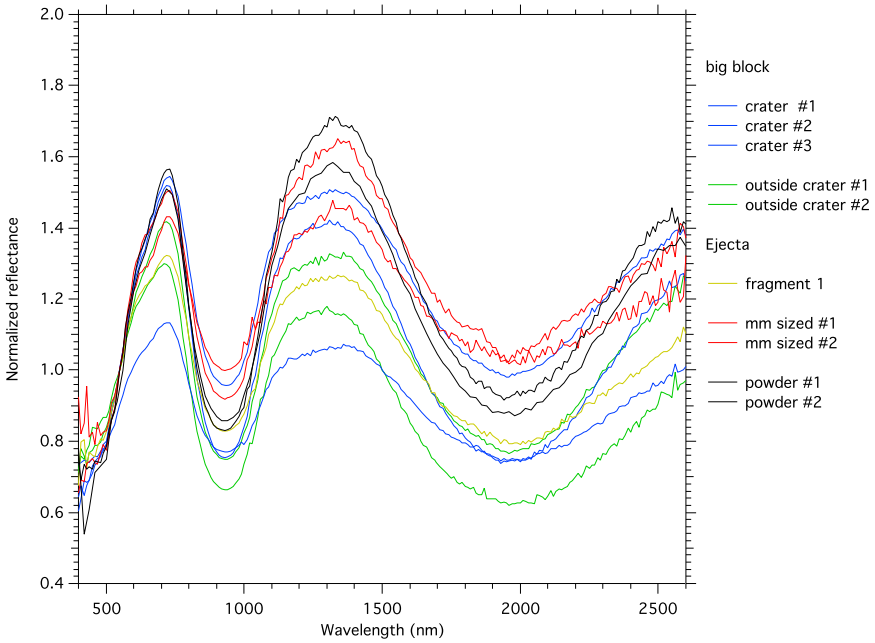

Figure 5. Normalized reflectance spectra of samples at 550 nm after being subjected to hypervelocity impacts, of craters, debris, and ejecta, as labeled.

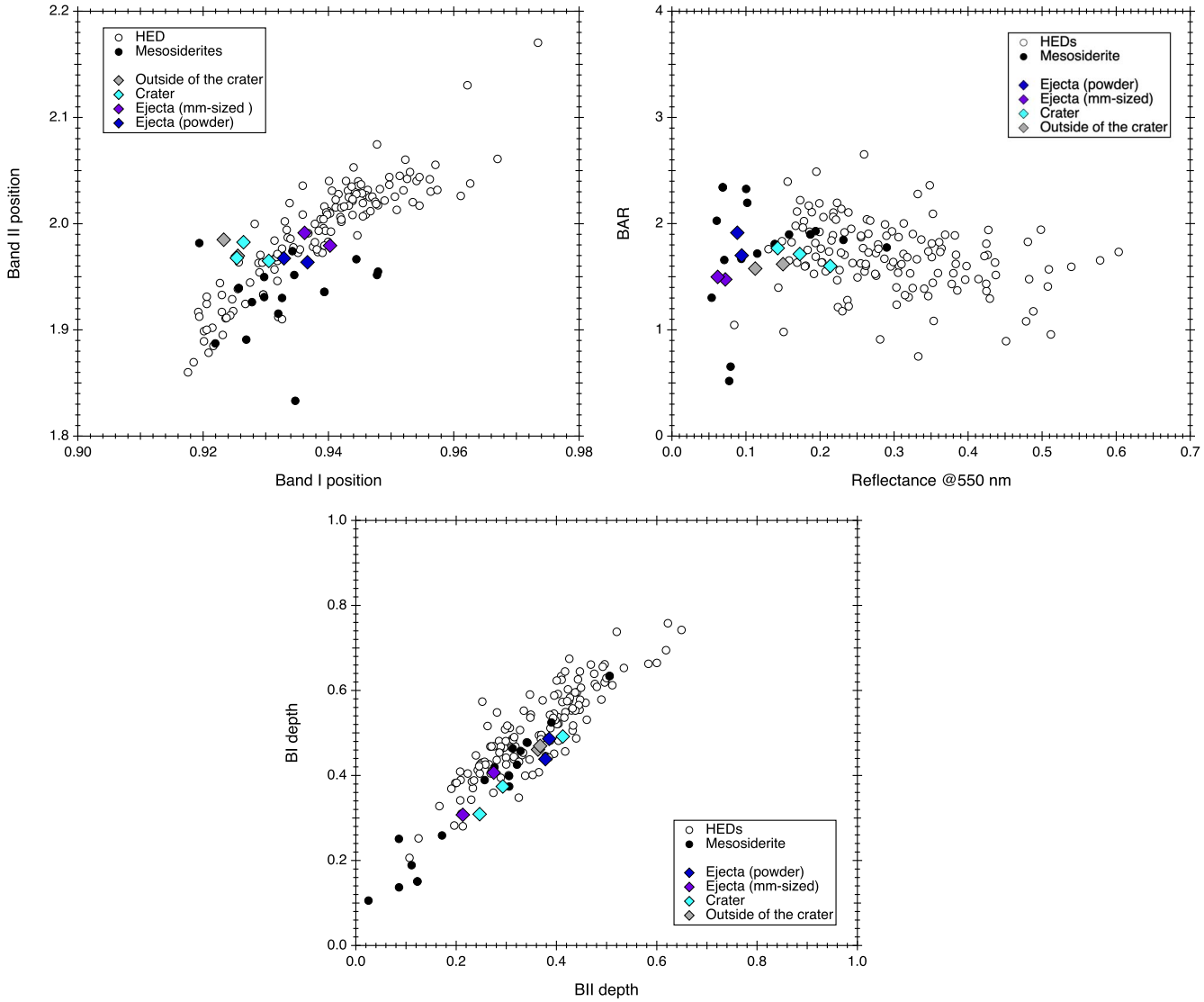

Figure 6. Spectral metrics of the crater, debris, and ejecta compared to those of mesosiderites and HED meteorites (see the references in the text).

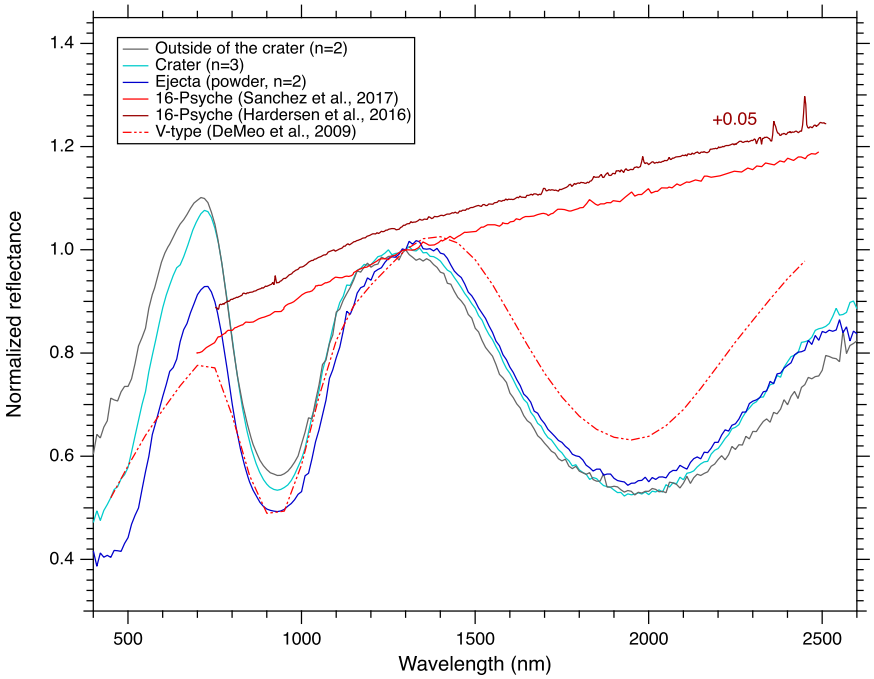

Figure 7. Comparison of the reflectance spectra obtained from the mesosiderite cratering experiment with those of Psyche (Hardersen et al. 2016; Sanchez et al. 2017) and of the V-type spectral end-member from DeMeo et al. (2009).

fraction of the surface of Psyche possibly being covered by mesosiderites, for example if basaltic materials were to have impacted its surface; the OSIRIS-REx mission revealed that exogeneous basaltic material, i.e., HED materials, can be present on the surface of a B-type asteroid (DellaGiustina et al. 2020).

To assess the amount of basaltic material that is required to explain the pyroxene signature of Psyche, we performed spectral mixing models between pure metal, and pure extraterrestrial basalt (an eucrite, Millbillillie; Figure 8). Both models (intimate or geographic mixture) reveal that only minute amounts of basaltic material (at the percent level) can explain this pyroxene signature. Such small fractions are in agreement with an exogeneous origin and the pyroxene signature observed on Psyche could be related to impacts of V-type-like material. This is one of the scenarios discussed in Hardersen et al. (2005). A small pyroxene modal proportion could also be the result of fast crystallization during the quenching of impact melts (Libourel et al. 2019).

4.3. Can the Bulk Psyche Be Related to Mesosiderites and What Are the Alternatives?

It appears that (16) Psyche has a surface that looks dominated by metals from reflectance spectra, but as a whole, Psyche hosts at least one constituent lighter than metal. Indeed, the density measurements of Psyche (3.89 ± 0.53 kg m^{-3}, Vernazza et al. 2021; 3.78 ± 0.34 kg m^{-3}, Elkins-Tanton et al. 2022) suggest a value that is incompatible with a metal-dominated asteroid (neither with a silicate-dominated object). Based on these density values, a mesosiderite origin has been argued for Psyche, but this hypothesis faces a few important challenges: (i) this requires a major impact between a large piece of Vesta (>100 km) and a differentiated object, in order to incorporate massive amounts of basaltic material within molten metal; (ii) the synchronicity of the metamorphic event that occurred on Vesta and the second peak in zircon ages measured for mesosiderites (Haba et al. 2019) would need to be fortuitous; and (iii) the reflectance spectra of Psyche are not compatible with a surface dominated by mesosiderites, and a surface process needs to occur to decrease and almost erase the optical signature of silicate, a scenario that appears unlikely.

Looking at the M-type population overall, there is a dichotomy based on the coupling of radar albedo and polarimetric properties (Belskaya et al. 2022). This dichotomy can be explained by the presence of enstatite chondrite–related objects and metal-rich objects within this class of asteroids (Belskaya et al. 2022), the two types of bodies being difficult to distinguish based on reflectance spectra alone. Several M types have a low radar albedo and relatively high |Pmin| values, including (21) Lutetia. The latter was visited by the ESA/Rosetta spacecraft and has a well-constrained density (3.4 ± 0.3; Sierks et al. 2011). Several strong arguments were given linking this asteroid to enstatite chondrites (Vernazza et al. 2011). Comparison to typical density values of enstatite chondrites (3.67 ± 0.07; Britt & Consolmagno 2003) implies a rather low value of the bulk porosity of (21) Lutetia (0%–15%). Such a level of macroporosity seems, however, a bit low for such a small body, which may hint at a differentiated interior (Vernazza et al. 2011, 2021; Weiss et al. 2012). A differentiated interior is also the likely case of M-type (22) Kalliope characterized by a density of $\rho = 4.40 \pm 0.46$ g cm^{-3}, so far the densest known small body of the solar system (Ferrais et al. 2022).

In the case of (16) Psyche, the density that can be derived from its radar albedo (about 3 to 4.6) is of the order of the density of the bulk object (Elkins-Tanton et al. 2022). If (16) Psyche is made of metal as a whole, then a large fraction of porosity should be present in the object as a whole (55%; Nichols-Fleming et al. 2022). The high-porosity model also implies that the asteroid remained cold after this high porosity was produced in some way, in order to avoid compaction (Nichols-Fleming et al. 2022). Most available observations of

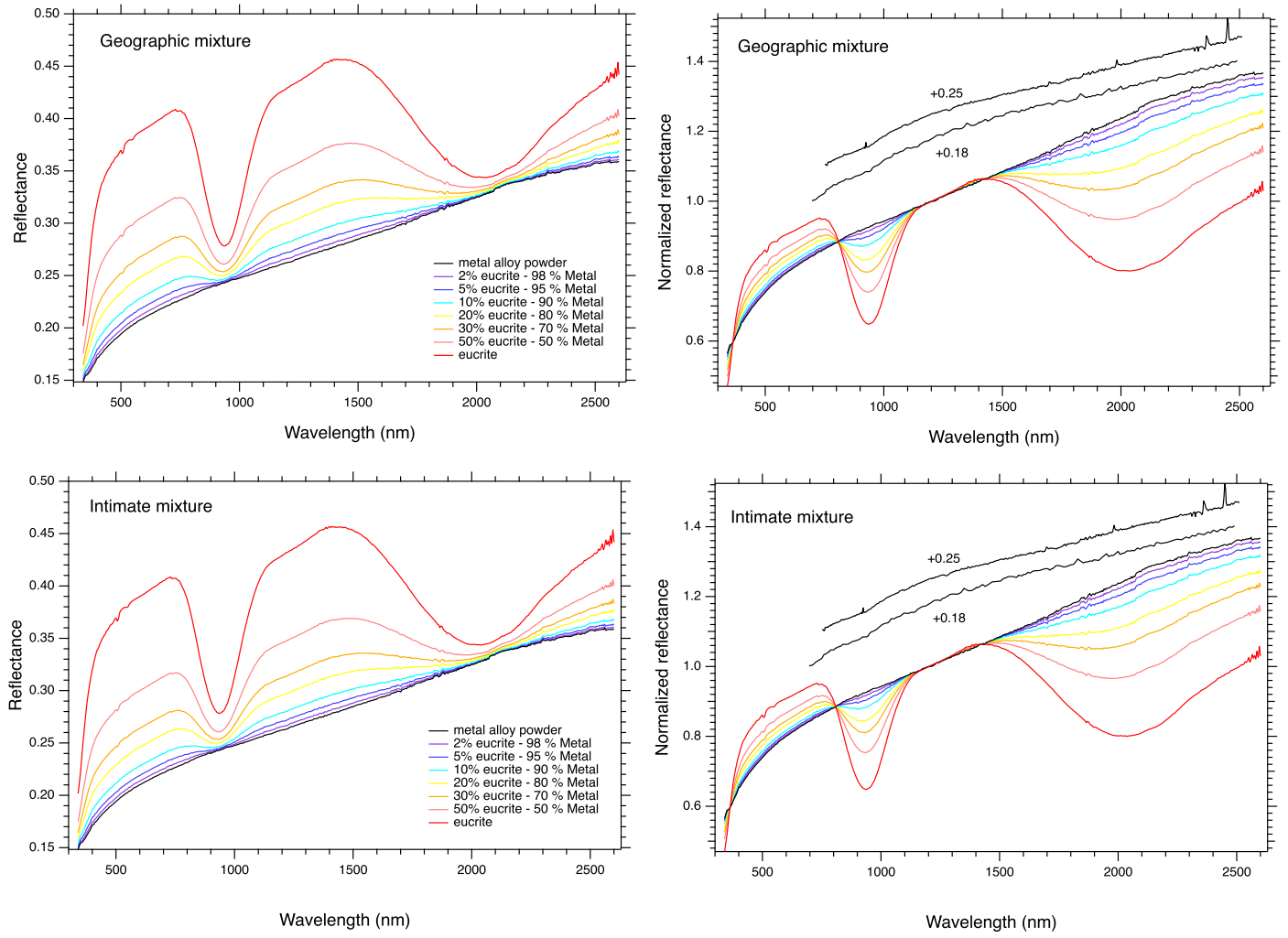

Figure 8. Spectral mixing models (intimate or geographic mixture) between pure metal, and pure extraterrestrial basalt (an eucrite, Millbillillie). the right column corresponds to normalized reflectance spectra of samples at 550 nm. Reflectance spectra of Psyche (Hardersen et al. 2016; Sanchez et al. 2017) are shown for comparison.

Psyche's surface are consistent with a metal-dominated regolith. The reflectance spectra are reminiscent of a metallic surface; their polarimetric properties are different from those of (21) Lutetia and of enstatite chondrites, whose radar albedo suggests a high density of the regolith in agreement with a metallic surface (using typical porosity values of asteroidal regolith). The difference with (21) Lutetia is that the bulk density of (16) Psyche seems similar to its surface/regolith density.

There are two possibilities to explain the bulk density of (16) Psyche. Either it hosts a significant fraction of bulk porosity (55%) as mentioned before, or it hosts a significant fraction of low-density (silicate) material. A high bulk porosity (55%) appears currently unlikely given the fact that similar-sized asteroids tend to possess average macroporosities in the 5%–20% range (Vernazza et al. 2021), including collisionally reaccumulated bodies. Zhang et al. (2022) have shown however that metallic asteroids may have high porosity due to cold welding between metal boulders and the high yield strength of metal for either ductile or brittle-like deformation.

If the global porosity of (16) Psyche is low (<20%), then it should be more silicate rich than metal rich as a whole. Looking at the correlation between iron content and density (Figure 9) among meteorites, we may expect a metal amount of about 40 wt% and then a silicate fraction of roughly 60 wt% if the bulk porosity is null. Metal-rich carbonaceous chondrites such as CH or CB have been suggested in the past as possible (16) Psyche analogs (Hardersen et al. 2005) and provide interesting alternatives to the pure metal hypothesis. In that case, a process is needed to enrich the surface of Psyche in metal to explain its optical properties and radar albedo. Little is known of the physical processes acting in the regolith of metal-rich objects, and mechanisms such as differential thermal cycling between metal and silicates, or the brazil-nut effect, may play a role. A last model would be that (16) Psyche and possibly some other M/X-type asteroids are made of a silicate core and a metal crust, i.e., an upside-down differentiated object. This would resolve the missing mantle problem among the suite of extraterrestrial samples and explain its metal-rich surface together with its rather low bulk density. But this model is at odds with the current view of planetary differentiation, except maybe if centrifugal forces were dominant in its early geodynamical history.

Ferrovolcanism, as proposed by Johnson et al. (2019), is a more plausible alternative for explaining the observations that asteroid (16) Psyche has a bulk density inconsistent with iron

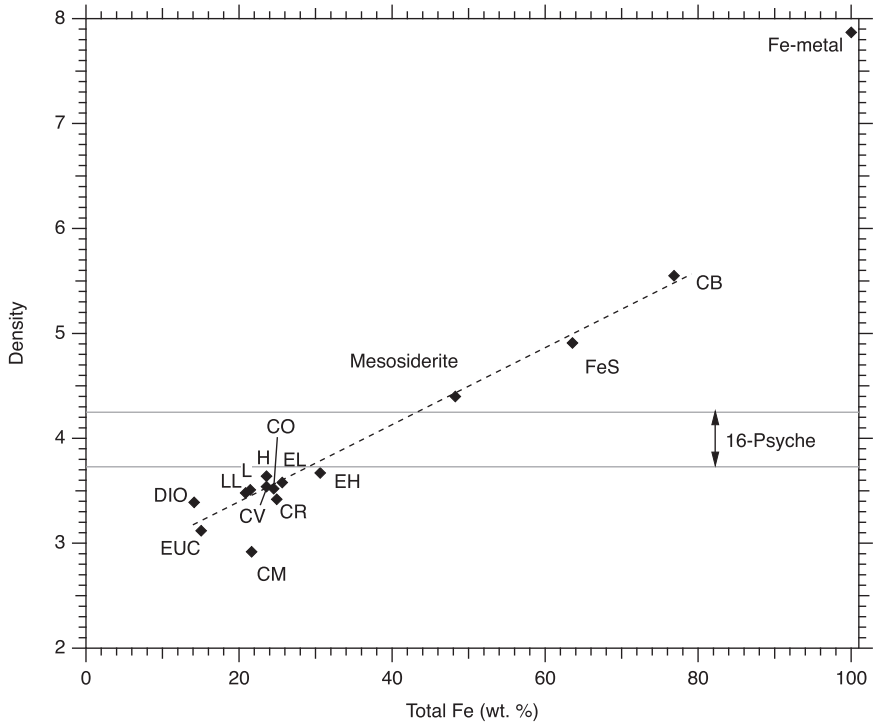

Figure 9. Density vs. iron weight fraction for selected meteorites groups of pure FeS and Fe metal. The density of (16) Psyche is from Viikinkonsky et al. (2018). The Fe contents are from Jarosewich (1990), except for the CR chondrite where the value is that of Renazzo (Weisberg et al. 1993) and CB chondrite where the value is that of Bencubbin (Lauretta et al. 2009). The density values for meteorites are grain density values from Britt & Consolmagno (2003) and Macke et al. (2011). The dotted line is a guide for the eye. The offset of the CM regarding that trend is related to the present of significant fraction of phyllosilicates.

meteorites and yet shows evidence of a metallic surface composition. This model, certainly applicable to other M/X-type asteroids, hints that regions of residual sulfur-enriched iron–nickel melt in the core attain sufficient excess pressures to propagate via dikes into the mantle and possibly even to erupt onto the planetesimal's surface, producing pallasite/mesosiderite-like metal–silicate assemblages.

4.4. Are Mesosiderites and HEDs Genetically Linked?

Today, most of the mass in the main belt is thought to have been dynamically implanted during an early evolutionary stage of the solar system, making the taxonomic classification of asteroids a key tool (Gradie & Tedesco 1982; DeMeo & Carry 2014; Mahlke et al. 2022). Among the several challenges posed to the grouping of objects with shared characteristics, the recognition of basaltic asteroids, as fragments of large bodies that went through the process of planetary differentiation, is a crucial one. If differentiated meteorites are easily distinguishable in our collections, the recognition of differentiated asteroids is more difficult since their few observable features are related to the partial mineralogy of their surfaces and their complex evolutions (e.g., by gardening, cratering, and/or space weathering).

The vis–NIR spectra of mesosiderites, HED meteorites, and V-type asteroids provides a good example. Similarities in the spectral signatures of HED achondrites and (4) Vesta in the inner main belt due to the same and prominent contribution of pyroxene led to early conclusions that Vesta is the parent body of these differentiated meteorites (e.g., McCord et al. 1970; Consolmagno & Drake 1977; Norton 2002). Mesosdiderite spectra collected before and after impact resemble to those of HED meteorites, both in terms of visible slope, band depth, and position of the 0.9 μm and 2.0 μm spectral features (Figures 6 and 7). As already noticed by previous works (Burbine et al. 2007; Wadhwa et al. 2003), this is going in the same direction of a genetic link between these two groups. The extremely close coincidence between the mean $\Delta^{17}O$ values for mesosiderites and HEDs (Greenwood et al. 2006) further strengthens this link. Complete oxygen isotopic homogenization appears to have been achieved in the HED parent body, indicating very high levels of melting and the development of a large magma ocean. This seems thus consistent with the assertion of mesosiderite formation on asteroid (4) Vesta by a hit-and-run collision (Haba et al. 2019).

However, if the great majority of HEDs have the same mean $\Delta^{17}O$ values ($\Delta^{17}O = -0.240 \pm 0.020‰$), some have been found clearly anomalous, suggesting the existence of multiple parent bodies for the ensemble of HED meteorites (Zhang et al. 2019). Isotopic studies of zinc (Paniello et al. 2012) and chromium (Benedix et al. 2017; Sanborn & Yin 2014) also suggested that HED meteorites are likely to originate from multiple differentiated/basaltic parent asteroids. This echoes the recognition of basaltic asteroids classified as V type in the middle and outer main belt (Mansour et al. 2018), assuming that if HEDs are from V-type asteroids then so are mesosiderites.

The existence of mesosiderite meteorites suggests there could be near-Earth asteroids with mesosiderite compositions. The discovery of the V-type asteroids near the resonance zone of the main belt solves the problem of the dynamical transfer mechanism of HED meteorites from Vesta to Earth, which is an important argument for the hypothesis that HED meteorites originate from Vesta (Binzel & Xu 1993). As an astrophysical perspective, it could be interesting to evaluate whether the V-type asteroids that are dynamically distinct from Vesta, or

different basaltic asteroids other than Vesta, have dynamical genetic connections with other resonances in the middle or outer main belt. As a cosmochemical perspective, the recognition of oxygen-anomalous mesosiderites may be important evidence for suggesting different parent asteroids for this meteorite class.

Since mesosiderites and HEDs are not composed of precisely the same material and that the optical properties are not enough to separate unambiguously both lithologies, the source of the mesosiderites, whether from (4) Vesta or other differentiated asteroids, still remains an important open question in planetary science.

5. Conclusion

Hypervelocity experiments on iron-rich materials at representative main asteroid belt impact speeds give invaluable insights on the evolution of regolith on iron-rich asteroids and on the response of these bodies to hypervelocity impacts. After our previous investigations of impacts on iron meteorites, this study presents the results of a campaign of hypervelocity impact experiments on natural mesosiderite targets.

We show:

1. The fragile behavior of mesosiderites at impact, since experiments result in both cratering and catastrophic disruption;
2. The influence of the original metal/silicate ratio on the ductile/fragile behavior of metal-rich asteroids at impact; and
3. The preservation of the initial vis–NIR spectral signature in impacted mesosiderites and their ejecta, which dominated by the spectra of pyroxene minerals characterized by their bands at 0.9 μm and 2 μm.

Our results thus rule out the mesosiderite hypothesis for the very nature of M/X-type asteroids including (16) Psyche, despite a small fraction of its surface possibly being covered by mesosiderite-like materials. Finally, we address the question of whether mesosiderites and HED meteorites are genetically linked to (4) Vesta and conclude that mesosiderites may well originate from other differentiated asteroids of the main belt.

Acknowledgments

This research was supported by the Hypervelocity Impact Facility (formerly Space Plasma Laboratory), ISAS, JAXA, Japan. The manuscript benefited from conversations with B. Carry and P. Tanga. We also thank the two anonymous reviewers for their constructive comments during the review process and Faith Vilas for editorial handling. The Fédération de Recherche Wolfgang Doeblin (FR 2800, CNRS), CNES, the CNRS through the MITI interdisciplinary program "Evenements Rares" (INSU, CNRS) and the European Union's Horizon 2020 research and innovation program under grant agreement No. 870377 (project NEO-MAPP) financially supported this research.

Author contributions: A.M.N. prepared the impact experiments and performed them and P.B. carried out the reflectance spectrometry of the impacted targets. G.L. and C.G. did the textural, chemical, and mineralogical characterization of the run samples. G.L., A.M.N., P.B., C.G., P.V., and P.M interpreted the data and contributed to data analysis. G.L. wrote the manuscript.

Competing interests: the authors declare that they have no competing interests. *Data and materials availability*: all data needed to evaluate the conclusions in the paper are present in the paper. Additional data related to this paper may be requested from the authors.

ORCID iDs

Akiko M. Nakamura https://orcid.org/0000-0001-6990-8496
Pierre Vernazza https://orcid.org/0000-0002-2564-6743
Patrick Michel https://orcid.org/0000-0002-0884-1993

References

Beck, P., Barrat, J.-A., Grisolle, F., et al. 2011, Icar, 216, 560
Belskaya, I., Berdyugin, A., Krugly, Y., et al. 2022, A&A, 663, A146
Benedix, G. K., Bland, P. A., Friedrich, J. M., et al. 2017, GeCoA, 208, 145
Binzel, R. P., & Xu, S. 1993, Sci, 260, 186
Bottke, W. F., Jr., Nolan, M. C., Greenberg, R., & Kolvoord, R. A. 1994, Icar, 107, 255
Britt, D. T., & Consolmagno, S. J. G. J. 2003, M&PS, 38, 1161
Burbine, T. H., Greenwood, R. C., Buchanan, P. C., Franchi, I. A., & Smith, C. L. 2007, LPSC, 39, 2119
Cambioni, S., de Kleer, K., & Shepard, M. 2022, JGRE, 127, e2021JE007091
Consolmagno, G. J., & Drake, M. J. 1977, GeCoA, 41, 1271
Davis, D. R., Farinella, P., & Marzari, F. 1999, Icar, 137, 140
de Kleer, K., Cambioni, S., & Shepard, M. 2021, PSJ, 2, 149
DellaGiustina, D. N., Burke, K. N., Walsh, K. J., et al. 2020, Sci, 370, eabc3660
DeMeo, F. E., Binzel, R. P., Slivan, S. M., & Bus, S. J. 2009, Icar, 202, 160
DeMeo, F. E., & Carry, B. 2014, Natur, 505, 629
Dollfus, A., & Geake, J. E. 1977, RSPTA, 285, 397
Dollfus, A., Mandeville, J.-C., & Duseaux, M. 1979, Icar, 37, 124
Drummond, J. D., Merline, W. J., Carry, B., et al. 2018, Icar, 305, 174
Elkins-Tanton, L. T., Asphaug, E., Bell, J. F., et al. 2022, SSRv, 218, 17
Ferrais, M., Jorda, L., Vernazza, P., et al. 2022, A&A, 662, A71
Ferrais, M., Vernazza, P., Jorda, L., et al. 2020, A&A, 638, L15
Flynn, G. J., Consolmagno, G. J., Brown, P., & Macke, R. J. 2018, ChEG, 78, 269
Fornasier, S., Clark, B. E., Dotto, E., et al. 2010, Icar, 210, 655
Ganino, C., Libourel, G., Nakamura, A. M., & Michel, P. 2019, P&SS, 177, 104684
Gradie, J., & Tedesco, E. 1982, Sci, 216, 1405
Greenwood, R. C., Franchi, I. A., Jambon, A., Barrat, J. A., & Burbine, T. H. 2006, Sci, 313, 1763
Grossman, J. 1999, M&PS, 34, A169
Haba, M. K., Wotzlaw, J.-F., Lai, Y.-J., Yamaguchi, A., & Schönbächler, M. 2019, NatGe, 12, 510
Hanuš, J., Viikinkoski, M., Marchis, F., et al. 2017, A&A, 601, A114
Hardersen, P. S. 2016, IRTF Asteroid NIR Reflectance Spectra V1.0. EAR-A-I0046-3-HARDERSENSPEC-V1.0. NASA Planetary Data System, https://pds.nasa.gov/ds-view/pds/viewDataset.jsp?dsid=EAR-A-I0046-3-HARDERSENSPEC-V1.0
Hardersen, P., Gaffey, M., & Abell, P. 2005, Icar, 175, 141
Hassanzadeh, J., Rubin, A. E., & Wasson, J. T. 1990, GeCoA, 54, 3197
Hiroi, T., Binzel, R. P., Sunshine, J. M., Pieters, C. M., & Takeda, H. 1995, Icar, 115, 374
Holsapple, K., Giblin, I., Housen, K., Nakamura, A., & Ryan, E. 2002, in Asteroids III, ed. W. F. Bottke, Jr. et al. (Tucson, AZ: Univ. Arizona Press), 443
Jarosewich, E. 1990, Meteoritics, 25, 323
Johnson, B. C., Sori, M. M., & Evans, A. J. 2019, NatAs, 4, 41
Jutzi, M., Holsapple, K., Wünneman, K., & Michel, P. 2015, in Asteroids IV, ed. P. Michel, F. E. DeMeo, & W. F. Bottke (Tucson, AZ: Univ. Arizona Press)
Katsura, T., Nakamura, A. M., Takabe, A., et al. 2014, Icar, 241, 1
Kawai, N., Tsurui, K., Hasegawa, S., & Sato, E. 2010, RScI, 81, 115105
Landsman, Z. A., Emery, J. P., Campins, H., et al. 2018, Icar, 304, 58
Lauretta, D. S., Goreva, J. S., Hill, D. H., et al. 2009, M&PS, 44, 823
Libourel, G., Nakamura, A. M., Beck, P., et al. 2019, SciA, 5, eaav3971
Macke, R. J., Britt, D. T., & Consolmagno, G. J. 2011, M&PS, 46, 311
Mahlke, M., Carry, B., & Mattei, P. -A 2022, A&A, 665, A26
Mansour, J. A., Popescu, M., & de León, J. 2018, EPSC, 12, 393

Marchi, S., Durda, D. D., Polanskey, C. A., et al. 2020, JGRE, 125, e05927
Marchi, S., Ermakov, A. I., Raymond, C. A., et al. 2016, NatCo, 7, 12257
Matsui, T., & Schultz, P. H. 1984, JGR, 89, C323
Maurel, C., Michel, P., Owen, J. M., et al. 2020, Icar, 338, 113505
McCord, T. B., Adams, J. B., & Johnson, T. V. 1970, Sci, 168, 1445
Michikami, T., et al. 2019, Icar, 331, 179
Mittlefehldt, D. W. 1990, GeCoA, 54, 1165
Mittlefehldt, D. W. 1994, GeCoA, 58, 1537
Moskovitz, N. A., Willman, M., Burbine, T. H., Binzel, R. P., & Bus, S. J. 2010, Icar, 208, 773
Nichols-Fleming, F., Evans, A. J., Johnson, B. C., & Sori, M. M. 2022, JGRE, 127, e07063
Norton, O. R. 2002, Choice Rev Online, 40, 40
Ockert-Bell, M. E., Clark, B. E., Shepard, M. K., et al. 2010, Icar, 210, 674
Ogawa, R., Nakamura, A. M., Suzuki, A. I., & Hasegawa, S. 2021, Icar, 362, 114410
Paniello, R. C., Moynier, F., Beck, P., et al. 2012, GeCoA, 86, 76
Pommerol, A., & Schmitt, B. 2008, JGR, 113, E10009
Potin, S., Brissaud, O., Beck, P., et al. 2018, ApOpt, 57, 8279
Raducan, S. D., Davison, T. M., & Collins, G. S. 2020, JGRE, 125, e2020JE006466
Rubin, A. E., & Mittlefehldt, D. W. 1992, GeCoA, 56, 827
Sanborn, M. E., & Yin, Q.-Z. 2014, LPSC, 45, 2018
Sanchez, J. A., Reddy, V., Shepard, M. K., et al. 2017, AJ, 153, 29
Scott, E. R. D., Haack, H., & Love, S. G. 2001, M&PS, 36, 869
Shepard, M. K., Clark, B. E., Ockert-Bell, M., et al. 2010, Icar, 208, 221
Shepard, M. K., Richardson, J., Taylor, P. A., et al. 2017, Icar, 281, 388
Shepard, M. K., Taylor, P. A., Nolan, M. C., et al. 2015, Icar, 245, 38
Sierks, H., Lamy, P., Barbieri, C., et al. 2011, Sci, 334, 487
Takir, D., Reddy, V., Sanchez, J. A., Shepard, M. K., & Emery, J. P. 2016, AJ, 153, 31
Vernazza, P., Binzel, R. P., Rossi, A., Fulchignoni, M., & Birlan, M. 2009, Natur, 458, 993
Vernazza, P., Ferrais, M., Jorda, L., et al. 2021, A&A, 654, A56
Vernazza, P., Lamy, P., Groussin, O., et al. 2011, Icar, 216, 650
Viikinkoski, M., Vernazza, P., Hanuš, J., et al. 2018, A&A, 619, L3
Wadhwa, M., Shukolyukov, A., Davis, A., Lugmair, G., & Mittlefehldt, D. 2003, GeCoA, 67, 5047
Wasson, J. T., & Rubin, A. E. 1985, Natur, 318, 168
Weisberg, M. K., Prinz, M., Clayton, R. N., & Mayeda, T. K. 1993, Geochimica et Cosmochimica Acta, 57, 1567
Weiss, B. P., Elkins-Tanton, L. T., Barucci, A. M., et al. 2012, P&SS, 66, 137
Zhang, C., Miao, B., & He, H. 2019, P&SS, 168, 83
Zhang, Z., Bercovici, D., & Elkins-Tanton, L. 2022, JGRE, 127, e2022JE007343